Meteoritics & Planetary Science 41, Nr 4, 553–570 (2006)
Abstract available online at http://meteoritics.org

The formation of plessite in meteoritic metal

J. I. GOLDSTEIN[1*] and J. R. MICHAEL[2]

[1]Department of Mechanical and Industrial Engineering, 313 Engineering Lab, University of Massachusetts, 160 Governors Drive, Amherst, Massachusetts 01003, USA
[2]Materials Characterization Department, Sandia National Laboratories, P.O. Box 5800, MS 0886, Albuquerque, New Mexico 87185, USA
[*]Corresponding author. E-mail: jig0@ecs.umass.edu

(Received 14 February 2005; revision accepted 04 November 2005)

Abstract–Plessite is a mixture of body-centered cubic (bcc) kamacite (α), face-centered cubic (fcc) taenite (γ), and/or ordered FeNi-tetrataenite (γ′) phases and is observed in the metal of iron, stony-iron, and chondritic meteorites. The formation of plessite was studied by measuring the orientation of the bcc and fcc phases over large regions of plessite using electron backscatter diffraction (EBSD) analysis in five ataxites, the Carlton IAB-IIICD iron, and zoneless plessite metal in the Kernouve H6 chondrite.

The EBSD results show that there are a number of different orientations of the bcc kamacite phase in the plessite microstructure. These orientations reflect the reaction path γ (fcc) → α_2 (bcc) in which the α_2 phase forms during cooling below the martensite start temperature, M_s, on the close-packed planes of the parent fcc phase according to one or more of the established orientation relationships (Kurdjumov-Sachs, Nishiyama-Wasserman, and Greninger-Troiano) for the fcc to bcc transformation.

The EBSD results also show that the orientation of the taenite and/or tetrataenite regions at the interfaces of prior α_2 (martensite) laths, is the same as that of the single crystal parent taenite γ phase of the meteorite. Therefore, the parent taenite γ was retained at the interfaces of martensite laths during cooling after the formation of martensite. The formation of plessite is described by the reaction $\gamma \rightarrow \alpha_2 + \gamma \rightarrow \alpha + \gamma$. This reaction is inconsistent with the decomposition of martensite laths to form γ phase as described by the reaction $\gamma \rightarrow \alpha_2 \rightarrow \alpha + \gamma$, which is the classical mechanism proposed by previous investigators. The varying orientations of the fine exsolved taenite and/or tetrataenite within decomposed martensite laths, however, are a response to the decomposition of α_2 (martensite) laths at low temperature and are formed by the reaction $\alpha_2 \rightarrow \alpha + \gamma$.

INTRODUCTION

Plessite is a mixture of body-centered cubic (bcc) kamacite (α), face-centered (fcc) taenite (γ), and/or ordered FeNi-tetrataenite (γ′) phases and is observed in the metal of iron, stony-iron, and chondritic meteorites. This two-phase mixture develops in the retained taenite of the metal as the host meteorite cools from high temperature. The microstructure of plessite is complex and, for the iron meteorites, is observed in a multitude of forms (pearlitic, spheroidized, acicular, comb, net, cellular, finger, black, duplex, and so on.), as described by Buchwald (1975). The microstructure is highly dependent on the local Ni content of the taenite (~7 to ~27 wt% Ni) in the characteristic "M" Ni profile, which develops during the nucleation and growth of the kamacite phase. Specific forms of plessite are observed in a chemical group of iron meteorites and are a function of the particular chemistry (Ni, P, and C content) and cooling rate of that chemical group. Figure 1 shows a variety of plessite microstructures with Ni contents from 10 to 25 wt%.

The formation of the plessite microstructure was described by Wood (1964) as the decomposition of metastable taenite (γ) to martensite (α_2) below the martensite start temperature (M_s) and the subsequent decomposition to a fine structure of α + γ, plessite, by the reaction:

$$\gamma \rightarrow \alpha_2 \rightarrow \alpha + \gamma \quad (1)$$

For example, when a typical metal particle of ~9 wt% Ni cools from the high temperature taenite (see Fig. 2), kamacite will form and the taenite will be enriched in Ni. When taenite of varying Ni content cools through the martensite start temperature, M_s, α_2 forms along the close packed planes of

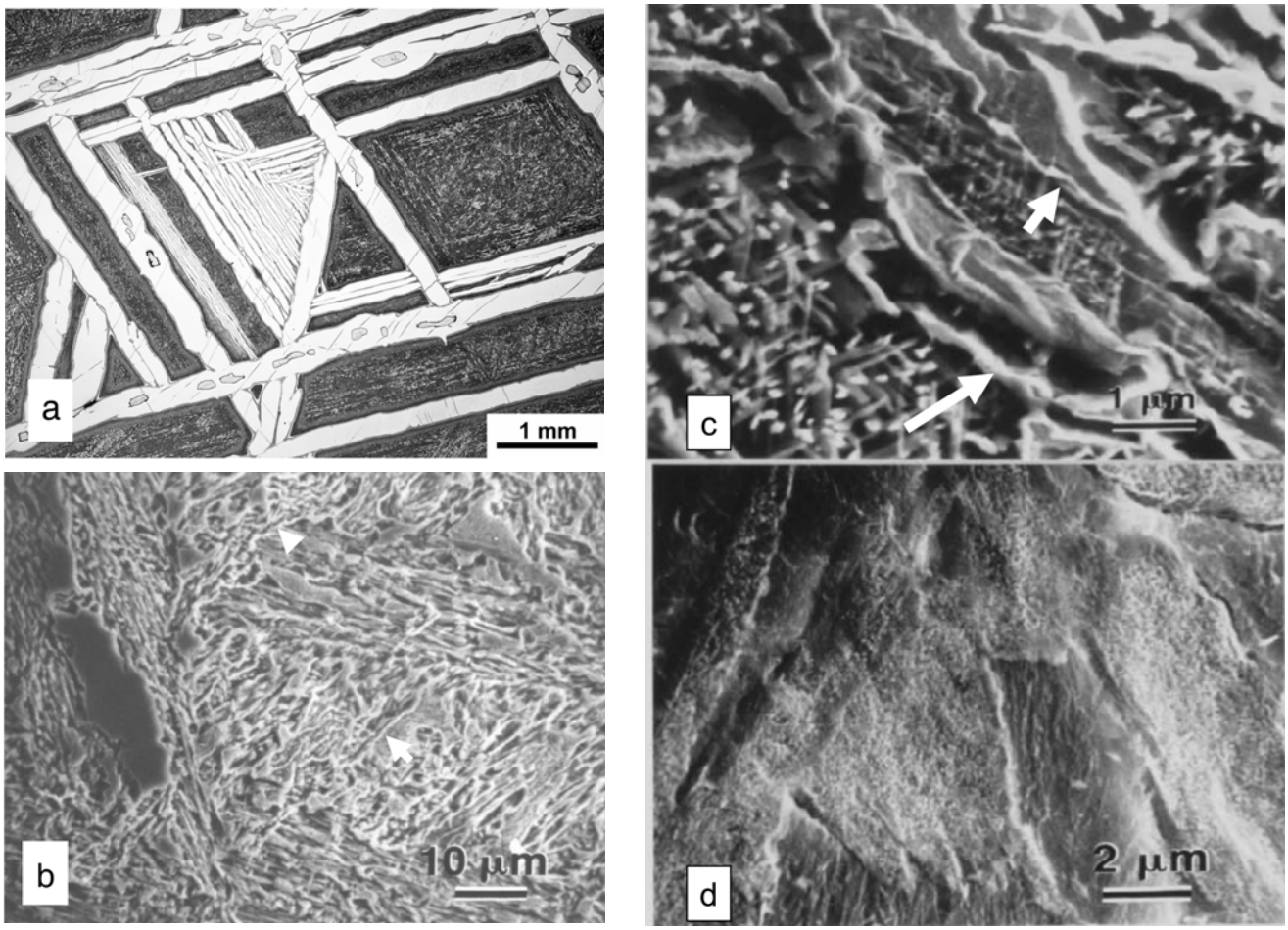

Fig. 1. a) The Carlton meteorite (13.3 wt% Ni). Plessite is the microstructure observed between the Widmanstätten plates. A region of microWidmanstätten plessite is observed near the center of the micrograph. b) An SEM image of duplex plessite in the Grant meteorite in a region of 10 wt% Ni. The arrows indicate martensite lath boundaries (Zhang et al. 1993). c) and d) SEM images of plessite regions in the Grant meteorite. (c) shows black plessite at ~20 wt% Ni. Precipitates have well-defined crystallographic orientations. The arrows indicate martensite lath boundaries. (d) shows very finely decomposed martensite at ~25 wt% Ni near the CT2 (clear taenite 2). Zhang et al. (1993).

the parent fcc taenite. Cooling proceeds and after the reaction, $\gamma \rightarrow \alpha_2$, is completed, α_2 martensite decomposes to $\alpha + \gamma$. The orientation of the γ phase in plessite will be controlled by the orientation of the parent α_2 martensite. At lower temperatures, taenite (γ) may transform to ordered FeNi-tetrataenite (γ''). If plessite is formed by Reaction 1, the orientation of the taenite-tetrataenite (γ-γ'') phase will be different from the orientation of the taenite in the original single-crystal taenite at high temperature.

Massalski et al. (1966) proposed that there are three types of plessites: types I, II, and III. Type I plessite forms at low Ni contents at or near the bulk Ni content of the meteorite and is observed microscopically as a microWidmanstätten pattern (acicular, comb, net, or finger plessite). A region of type I plessite is shown in Fig. 1a for the Carlton meteorite. Type I plessite forms by the same mechanism that controls the primary Widmanstätten pattern formation as recently described by Yang and Goldstein (2005). Type II plessite has a plate martensitic appearance, has a high Ni content (25 to 29 wt% Ni) and is observed at the border with undecomposed taenite. According to Massalski et al. (1966), the structure forms at low temperature by the reaction $\gamma \rightarrow \alpha_2$. More recent TEM and SEM investigations have shown that type II plessite has decomposed to a mixture of $\alpha + \gamma$ (see Fig. 1d or Fig. 12) (Zhang et al. 1993). Massalski et al. (1966) characterized type III plessite as a more or less even distribution of γ and α particles formed by Reaction 1. The composition of type III plessite falls between that of type I and type II plessite. Type III plessite is proposed to form by the same reaction as postulated by Wood (1964), in which taenite is fully transformed to martensite (α_2) before decomposition to $\alpha + \gamma$.

Zhang et al. (1993) studied the microstructure of plessite in two iron meteorites (Grant IIIAB and Carlton IAB-IIICD) using scanning and transmission electron microscopy. They discuss a continuum of plessite microstructures that vary with Ni content (~10 to >25 wt%). At low Ni, a duplex plessite structure of taenite (γ) and/or ordered tetrataenite (γ'') regions are present along prior α_2 boundaries (see Fig. 1b). At Ni

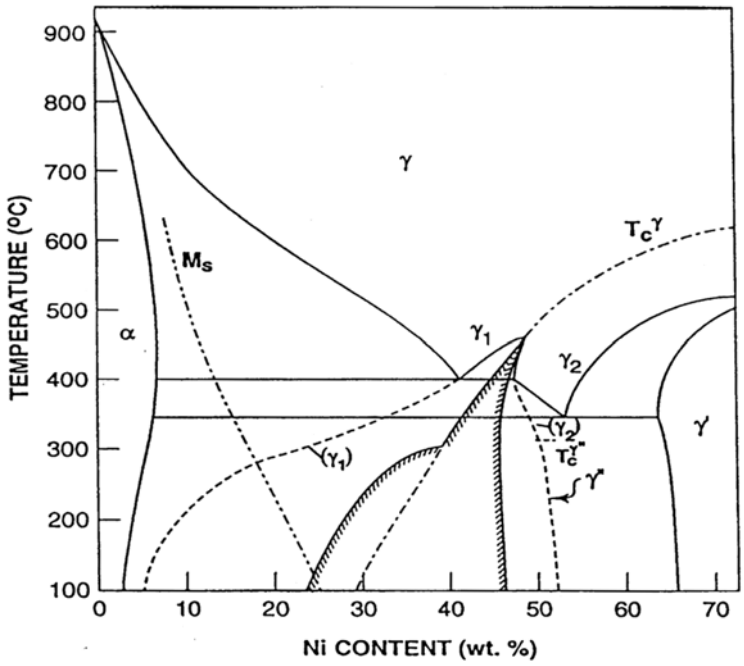

Fig. 2. An Fe-Ni binary phase diagram (Yang et al. 1996). α is a low Ni bcc phase, γ is a high Ni fcc phase, γ_1 is a low Ni paramagnetic fcc phase, γ_2 is a high Ni ferromagnetic fcc phase, γ′ is ordered Ni_3Fe, γ″ is ordered FeNi-tetrataenite, and M_s is the martensite starting temperature. T_c^{γ} is the Curie temperature of the γ phase, and $T_c^{\gamma''}$ is the ordering temperature of FeNi, γ″.

contents greater than about 13 to 14 wt%, fine taenite and/or tetrataenite (γ–γ″) regions are present not only along prior α_2 boundaries, but also as exsolution lamellae, typically ~10–20 nm wide, within the prior α_2 matrix. At high Ni contents (~20 wt% Ni), a large number of fine precipitates are observed (see Fig. 1c). The high Ni plessite structure is called black plessite.

Zhang et al. (1993) argued that Reaction 1, which is the same reaction proposed by Massalski et al. (1966) for type III plessite, is responsible for the formation of the continuum of plessite microstructures. According to Zhang et al. (1993), as the Ni content of the plessite microstructure increases, lath martensite (α_2) forms at lower and lower temperatures. None of the original taenite of the parent phase of the meteorite is retained. Correspondingly, the formation of taenite and/or tetrataenite regions at lath martensite (α_2) boundaries decreases with decreasing temperature and the nucleation of taenite and/or tetrataenite precipitates (exsolution lamellae) within the original martensite (α_2) laths increases. If the plessite microstructure developed, as described by Zhang et al. (1993), the γ–γ″ regions at the lath boundaries and the exsolution lamellae in prior martensite (α_2) laths have a different orientation than that of the single crystal parent taenite phase of the meteorite.

In a recent study, Yang and Goldstein (2005) discussed several reactions for the formation of the plessite structure: 1) Reaction 1 controls the formation of the fine plessite microstructure such as black plessite (Zhang et al. 1993) with Ni contents much above the Ni content of the host metal. All the parent γ is converted to martensite (α_2) on cooling. The taenite and/or tetrataenite that is formed has a different orientation from the parent γ phase of the meteorite, since the γ precipitates exsolve from an α_2 matrix. This is the same mechanism postulated by Massalski et al. (1966) for type III plessite. 2) Reaction 2, which is:

$$\gamma \rightarrow \alpha_2 + \gamma \rightarrow \alpha + \gamma \quad (2)$$

controls the formation of lower Ni plessite such as duplex plessite. For this mechanism, some of the parent taenite phase is retained at martensite boundaries (Fig. 1b) to low cooling temperatures and has the same orientation as that of the single crystal parent taenite phase of the meteorite. 3) Reaction 1 controls the formation of high Ni taenite (~25 wt%) in which martensite (α_2) forms at low temperatures, and the $\alpha + \gamma$ occurs on a very fine scale. These high Ni plessite regions are type II plessite as described by Massalski et al. (1966).

The purpose of this study is to sort out the two reactions that have been proposed to control the formation of plessite as a function of taenite Ni content. The two reactions can be clearly differentiated if one can measure the orientation of taenite and/or tetrataenite at the martensite lath boundaries and within the martensite laths of the plessite structure and can measure the orientation of taenite from the original meteorite single crystal metal.

Measurements of orientation relationships between taenite and/or tetrataenite and kamacite at prior martensite α_2 lath boundaries have been made using transmission electron microscope (TEM) techniques in Grant IIIAB and Carlton

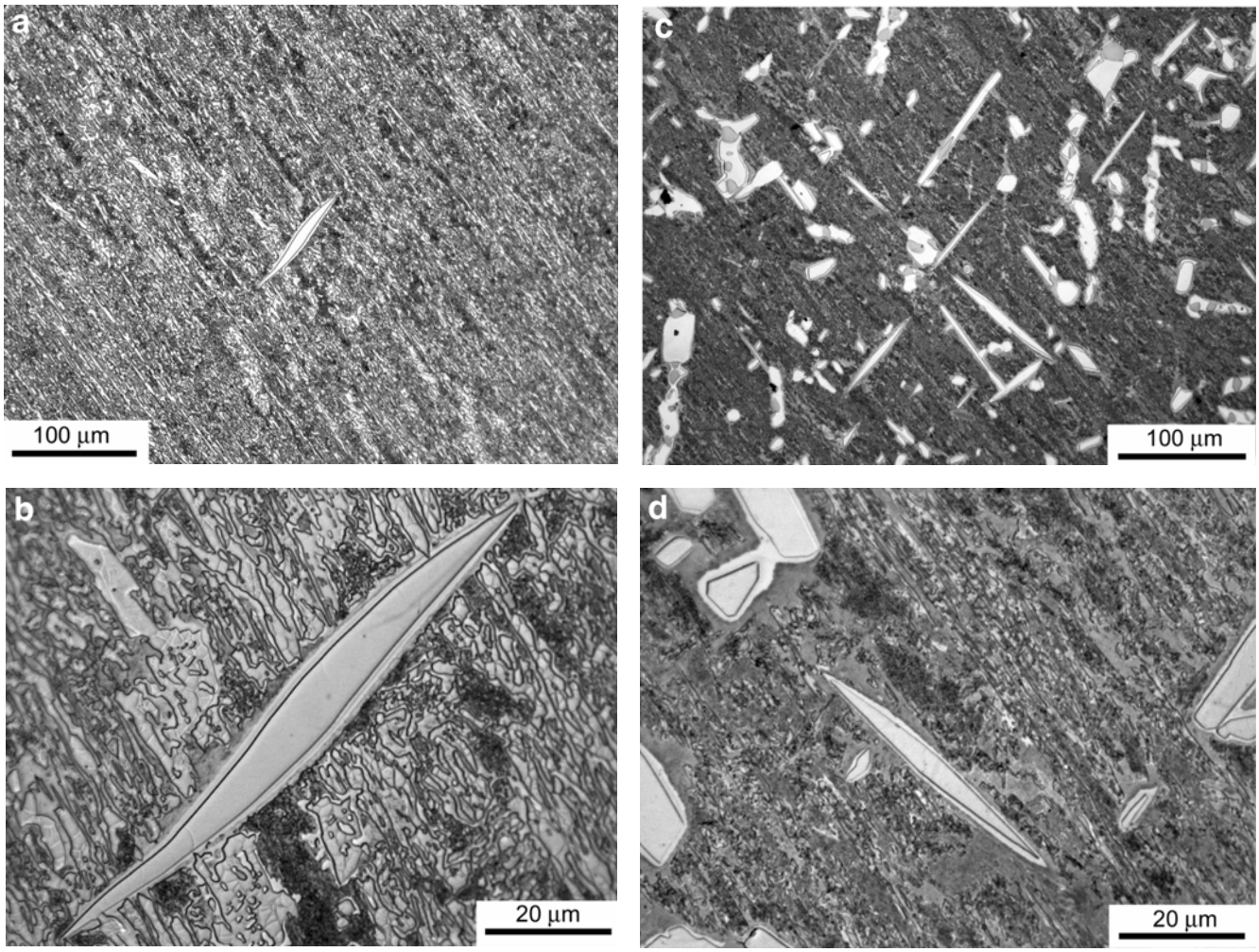

Fig. 3. Light optical micrographs of two polished and etched IVB meteorites. a) Cape of Good Hope, low magnification. b) Cape of Good Hope, high magnification. c) Weaver Mountains, low magnification. d) Weaver Mountains, high magnification. The ataxite structure consists of occasional kamacite (α-bcc) plates in a plessite matrix. Phosphides are surrounded by kamacite in the microstructure of Weaver Mountains.

IIICD, Zhang et al. (1993). These authors found that taenite and/or tetrataenite is present at α_2 boundaries and that the fcc {111} planes of the γ phases are parallel to the bcc {110} planes of the kamacite (prior martensite laths). The orientation relationship could be either Nishiyama-Wassermann or Kurdjumov-Sachs. However, because TEM electron diffraction data are obtained from a limited area (~1 μm^2), it was not possible to determine if the orientation of the taenite and/or tetrataenite at martensite (α_2) boundaries is the same or different from the orientation of the original taenite single crystal. In addition, Zhang et al. (1993) measured the orientation of the fine 10–100 nm wide γ–γ′ exsolution plates in martensite (α_2) laths (Zhang et al. 1993) (Fig. 1c) using the TEM. These γ–γ′ plates had a fcc crystal structure with {111} planes parallel to one of the {110} planes of the kamacite which formed from decomposed martensite laths.

We use the technique of electron backscatter diffraction (EBSD) to obtain crystallographic information on the orientation of the α and γ–γ′ phases over large regions of the plessite microstructure. The EBSD technique has been used very recently by a number of investigators to study orientation relationships between taenite and kamacite in iron meteorites and, in some cases, orientation relationships in plessite. For example, Nolze and Geist (2004) investigated bcc-fcc orientations in the plessite of three iron meteorites. Hutchinson and Hagström (Forthcoming) and He et al. (2005) studied orientation relationships in the Gibeon meteorite. However, none of the observations obtained in these papers were used to develop an understanding of the microstructural evolution of plessite in meteorites during the cooling process.

The IVB ataxites are investigated in detail in this study since the microstructure of this chemical group of iron meteorites is plessite that contains a few kamacite plates ~6–30 μm in width (Buchwald 1975). As shown in Fig. 3, the

Table 1a. The composition of metal in the meteorites analyzed in this study.

		USNM No.	Ni (wt%)	Co (wt%)	P (wt%)
Cape of Good Hope	IVB	2706	16.32, 15.64[a]	0.84, 0.782[a]	0.12, 0.0445[a]
Hoba	IVB	3390	16.4, 16.33[a]	0.76, 0.781[a]	0.07, 0.0757[a]
Chinga	Ungrouped	1585	16.58	0.55	0.05
Tawallah Valley	IVB	1458	17.6, 17.94[a]	0.69, 0.816[a]	0.1, 0.176[a]
Weaver Mountains	IVB	1624	17.72	0.82	0.1
Carlton	IIICD	152	13.3[b]	0.53[c]	0.6[b]
Kernouve	H6	2211	9.8[d]	0.45[d]	<0.02[d]

[a]Campbell and Humayun (2005).
[b]Analysis from Buchwald (1975).
[c]Moore and Lewis (1968).
[d]Average composition of zoneless plessite particles, Reisener and Goldstein (2003).

Table 1b. The mechanism for Widmanstätten pattern formation in meteorites analyzed in this study (Yang and Goldstein 2005).

Cape of Good Hope	IVB	$\gamma \rightarrow (\alpha + \gamma) \rightarrow \alpha + \gamma + Ph$
Hoba	IVB	$\gamma \rightarrow (\alpha + \gamma) \rightarrow \alpha + \gamma + Ph$
Chinga	Ungrouped	$\gamma \rightarrow \gamma + Ph \rightarrow \alpha + \gamma + Ph$[a]
Tawallah Valley	IVB	$\gamma \rightarrow \gamma + Ph \rightarrow \alpha + \gamma + Ph$
Weaver Mountains	IVB	$\gamma \rightarrow \gamma + Ph \rightarrow \alpha + \gamma + Ph$
Carlton	IIICD	$\gamma \rightarrow \gamma + Ph \rightarrow \alpha + \gamma + Ph$

[a]P is probably higher than the value given in Table 1a.
γ = taenite, α = kamacite, and Ph = phosphide.

ataxite structure consists of occasional kamacite (α-bcc) spindles or rods (Cape of Good Hope, Figs. 3a and 3b) or kamacite in a Widmanstätten orientation (Weaver Mountains, Figs. 3c and 3d) within a matrix of plessite, a fine-grained intergrowth of kamacite and taenite and/or tetrataenite. Jago (1981) and Novotny et al. (1982) have studied the microstructure of ataxites using scanning electron microscopy (SEM) and transmission and analytical electron microscopy (TEM-AEM). Novotny et al. (1982) have shown that the IVB ataxites have a type III plessite microstructure (Massalski et al. 1966) consisting of fine rods of a face-centered cubic phase in a body-centered cubic kamacite matrix. No ordered FeNi (tetrataenite), γ', was observed in their study.

The EBSD technique allows for a clear delineation of crystallography as well as orientation relationships in the IVB meteorites. We will show that, in contrast to previous studies, Reaction 2 is applicable for the formation of both duplex and black plessite, from ~10 to >18 wt% Ni, and that the parent γ phase is retained from high temperatures at the martensite lath boundaries.

Since the plessite microstructure, which is a function of Ni content, is the same in meteoritic metal of chondrites, stony irons, and irons, the results of this study are widely applicable to plessite formation in all types of meteorites. We test this assumption by studying the crystallography and orientation relations of the plessite microstructure in Carlton, a IIICD iron, and in Kernouve, a H6 chondrite.

PROCEDURE

Four IVB irons (Cape of Good Hope, Hoba, Tawallah Valley, and Weaver Mountains) and an ungrouped iron, Chinga, which has a similar microstructure, were examined in this study. The microstructure of these meteorites contains a mixture of duplex and black plessite with a few kamacite plates ~6–30 μm in width (Buchwald 1975). The mechanism for the formation of the kamacite plates in each meteorite is given in Table 1. The Ni, Co, and P contents of these meteorites (Buchwald 1975) are given in Table 1a along with more recent values from laser ablation inductively-coupled plasma mass spectrometry (Campbell and Humayun 2004). Plessite in Carlton, a IAB-IIICD iron, and in a zoneless plessite particle in Kernouve, a H6 chondrite, was also examined (Table 1). The mechanism for the formation of the Widmanstätten pattern in the high P containing Carlton iron is also given in Table 1b.

Meteorite samples were first examined by optical microscopy and scanning electron microscopy after standard metallographic polishing and etching with 2% nital. The samples were then repolished for EBSD investigation. Successful application of EBSD required that the sample surface be clean and relatively flat and free of preparation-induced damage. The samples were polished using standard metallographic polishing procedures followed by a two-step vibratory polishing procedure. The first vibratory polishing was performed using 0.1 μm Al_2O_3 for 4 hr and was followed by a second vibratory polishing step using 0.04 μm SiO_2 for 2–4 hr. The vibratory polishing produced both a mechanical polishing effect and a chemical polish that helped develop very smooth surfaces. Both steps were carried out on napped cloth. This procedure produced samples that had minimal surface relief between the kamacite and taenite and were free of specimen preparation-induced damage.

Electron backscatter diffraction (EBSD) studies of plessite in meteoritic metal were accomplished using a ZEISS Supra 55VP field emission SEM outfitted with an EBSD unit from HKL Technology, with Channel 5 software. Orientation maps of the fcc and bcc in plessite regions from meteorite

samples listed in Table 1 were obtained. Some of the meteorites contained tetrataenite (γ''), which had ~50 at% Ni and is an ordered phase with a primitive tetragonal unit cell and lattice parameters: $a = 0.35761$ nm, $c = 0.3589$ nm ($c/a = 1.0036$) (Albertsen 1981). Ordering caused a very small distortion of the parent taenite structure (c/a of 1.0036) so that, in using the EBSD technique, the diffraction pattern from tetrataenite (γ'') was indistinguishable from fcc taenite. EBSD orientation maps were collected using a beam voltage of 20 kV, a beam current of about 1–2 nA, and a focused probe size of less than 2 nm in diameter. The sample was tilted 62° from the horizontal for orientation mapping.

EBSD mapping was performed in the following manner: The electron beam was sequentially placed pixel by pixel across the area to be mapped. The pixel spacing was selected so that the microstructure to be mapped was adequately sampled. The pixel spacing varied from 0.02 to 0.5 μm per pixel. At each pixel, the beam was stopped and an EBSD pattern collected. The location of at least five bands in the EBSD pattern was obtained through the use of the Hough transform and the angles between the bands were calculated. The angles between the bands were then checked against crystallographic descriptions of taenite (γ, a fcc structure) or kamacite (α, a bcc structure). Although both kamacite and taenite are cubic, it was relatively easy to discriminate between the two crystal structures. Since kamacite was bcc and taenite was fcc, there are differences in the planes that appear in the electron diffraction patterns due to systematic absences that can be determined from simple structure factor determinations caused by interference effects. When a consistent set of angles between planes was found, the diffraction pattern was indexed as either kamacite or taenite and the orientation of that pixel with respect to the sample frame of reference was determined. In this case, the frame of reference used was that the sample surface is normal to the Z direction. The direction normal to the Z direction, in the plane of the sample surface and parallel to the sample tilt axis, was the X direction and the normal to both the X and Z directions was the Y direction. Thus, at every pixel the crystallographic structure was identified and the complete orientation matrix was determined.

The procedure described above is repeated at every pixel throughout the area of interest at a rate of about 20 pixels per second. A map of 1000 × 850 pixels with a pixel spacing of 0.1 μm covered an area on the sample of 100 μm × 85 μm and required about 12 hr to complete. A pixel spacing of 0.1 μm (100 nm) was small enough to observe the orientation of fcc along prior α_2 boundaries, but was too large to observe the orientation of exsolved fcc of ~10–20 nm thickness within the prior α_2 matrix. Measurements using a pixel spacing of 0.02 μm (20 nm) were small enough to also observe the orientation of fcc within the prior α_2 matrix. A review of EBSD and its application to orientation determination is given by Schwartz et al. (2000).

The orientation information collected during an EBSD scan may be presented as either orientation maps or standard pole figures. Orientation maps, also called inverse pole figure maps because only one reference direction may be shown in any one map, are color-keyed with respect to the orientation of a given pixel. Thus, any pixels with the same orientations are colored the same. Infrequently, there are EBSD patterns that cannot be consistently indexed as either fcc or bcc, and as a result, some pixels are shown in black. There are a variety of reasons for this lack of indexing, for example, surface roughness, spatial resolution limitations, or the presence of other phases (e.g., phosphides or sulfides) that are not included in the list of crystallographic descriptions of possible phases. It is also possible to use a measure of the sharpness of the EBSD pattern (called band contrast) to show the microstructure of the sample in grayscale. Band contrast images are simple measures of the quality of the diffraction patterns that are collected: the higher the band contrast, the better the diffraction pattern. Diffraction patterns from deformed regions and grain boundaries are usually less well-defined and have lower band contrast values. Grain boundaries have lower band contrast due to the overlap between the diffraction patterns on either side of the boundary. The actual band contrast value can be derived from the ratio of the average intensity of the Kikuchi bands to the average intensity for the entire pattern. These images are remarkably clear and difficult to distinguish from grayscale SEM images. Since EBSD determines the complete orientation matrix of the crystal at each pixel in the image, it was also possible to plot this information as pole figures with respect to some external frame of reference. In the case of metal processing, for example, there are standard reference directions related to the materials processing. In the case of meteorites, there are no meaningful reference directions.

The resolution of EBSD mapping has improved markedly with the introduction of the field emission SEM (FESEM). Humphreys et al. (1999) and Humphreys (2002) have shown EBSD spatial resolutions of better than 15 nm (0.015 μm) in Al and better than 10 nm (0.010 μm) in Cu-Zn alloys using an FESEM. In each of these studies, the samples were prepared using standard metallographic techniques that usually involve final polishing with colloidal silica media. Sivel et. al. (2005) have reported EBSD spatial resolutions approaching a few nm in samples prepared using focused ion beam techniques.

RESULTS

Figures 4a–c show band contrast as well as bcc and fcc orientation maps for the Cape of Good Hope ataxite, covering an area of about 100 × 85 μm^2. Figure 4d shows a typical color legend based on the stereographic triangle. The bcc phase shown in Fig. 4b has multiple orientations, presumably from the reaction for the formation of martensite (α_2) on

cooling. The martensite (α_2) is distorted bcc when it is formed below the martensite start temperature, M_s (Fig. 2). Figures 4e–h display fcc orientation maps covering areas of about 100 × 85 μm^2 for Chinga, Hoba, Tawallah Valley, and Weaver Mountains. For each meteorite, taenite and/or tetrataenite (γ–γ′) regions of plessite are found along prior α_2 boundaries. For Cape of Good Hope, Chinga, Tawallah Valley, and Weaver Mountains, the orientation maps also include kamacite spindles in a Widmanstätten orientation. For these samples, the γ–γ′ regions along prior α_2 boundaries have the same orientation as the taenite phase (original taenite phase orientation) surrounding the kamacite plates. Therefore, taenite and/or tetrataenite regions along prior α_2 boundaries in plessite have the same orientation as the single crystal parent taenite phase of the meteorite.

Figures 5 and 6 show fcc orientation maps of Chinga in a small region 16 μm × 13 μm and of Tawallah Valley in a small region 14 μm × 12 μm, respectively. At this magnification, the pixel size is ~20 nm, which allows the measurement of the orientation of γ–γ′ phases both along prior α_2 boundaries and within decomposed α_2 laths. The fcc regions along prior α_2 boundaries have the same orientation. For example, the fcc orientation is within ~7^0, resulting in a pink to purple color change for Chinga and a pink to rose color change for Tawallah Valley. Some of the fine exsolved γ–γ′ within the decomposed α_2 laths have different orientations. For example, exsolved γ–γ′, indicated by the arrows in Figs. 5 and 6, have orientation variations of 10° or more. The varying orientations of the fine exsolved γ–γ′ are a response to the decomposition of martensite α_2 laths at low temperature.

The bcc phase in each of the five ataxites has a number of different orientations (e.g., Fig. 4b, the bcc orientation map for Cape of Good Hope). These orientations reflect the fact that the α_2 phase forms on the close-packed planes of the parent taenite. The Kurdjumov-Sachs (K-S), Nishiyama-Wassermann (N-W), and the Greninger-Troiano (G-T) orientation relationships are shown in Table 2. There are 24 possible variants of the K-S orientation relationship and 12 variants for the N-W orientation relationship, as discussed in Guo (2004). Figure 7 shows pole figures obtained from Tawallah Valley (Fig. 4g). Figures 7a–c are the {100}, {110}, and {111} pole figures for the bcc phase and Fig. 7d is the {111} pole figure for the fcc phase. The fcc pole figure of Fig. 7d shows that nearly all of the fcc phase that was detected has the same orientation. The remainder of the fcc orientations (Fig. 7d) is obtained from some of the larger fcc laths that have exsolved from the super-saturated bcc (α_2) phase by the reaction $\alpha_2 \rightarrow \gamma + \alpha$. The bcc pole figures show the arrangement of the bcc phase variants that are present and include both the bcc phase in the Widmanstätten plates and the bcc phase in the martensite that formed. Additional orientation maps and pole figures were obtained from plessite in Tawallah Valley. The fcc phase has the same orientation as the area shown in Fig. 4g.

Figure 8 shows pole figures calculated from the Kurdjumov-Sachs (K-S) and the Nishiyama-Wassermann (N-W) orientation relationships (Table 2). These pole figures show graphically the orientation relationship given in Table 2. For example, a comparison of the {111} pole figure of fcc in Fig. 8d with the {110}pole figure of bcc in Fig. 8c shows that the {111} plane in fcc are coincident with the {110} plane in bcc. Figure 8a shows the pole figures expected for the K-S orientation relationship. Figure 8b shows the pole figures that are expected for the N-W orientation relationship and Fig. 8c shows the combined pole figures for K-S and N-W. The experimental pole figures, Fig. 7, show reasonable agreement with the calculated pole figures of Fig. 8. As shown in Fig. 8, it is difficult to distinguish among K-S, N-W, or the G-T orientations. In summary, the bcc pole figures in Figs. 7 and 8 would only be formed when the bcc phase has transformed from a single orientation of the parent fcc phase.

Figure 1a shows an optical micrograph and Fig. 10a shows a fcc orientation map of the Carlton IIICD iron meteorite in a region of about 55 μm × 45 μm. As in the ataxites, the orientation of the fcc phase is essentially the same for all γ–γ′ phases along prior α_2 boundaries and is the same as the original taenite single crystal surrounding a major Widmanstätten kamacite band. Some of the exsolved γ–γ′ (see arrows in Fig. 10a) are observed within the decomposed α_2 laths and have different orientations than the original taenite single crystal of the meteorite. The exsolved γ–γ′ formed by the decomposition of martensite (α_2) laths at low temperature (Zhang et al. 1993). As in the ataxites, the kamacite has a number of different orientations reflecting the reaction path for the formation of the martensite (α_2) microstructure. Figure 11 displays pole figures obtained from the fcc and bcc orientation maps of Carlton. The experimental pole figures in Fig. 11 are not in the same orientation as the calculated pole figures shown in Fig. 8. However, the orientation relationships are still apparent in Fig. 11. These pole figures are similar to those shown in Fig. 7 from Tawallah Valley and are consistent with the orientation relationships shown in Table 2. The scatter in the fcc pole figure, Fig. 11d, is most likely due to the observation of a limited number of the larger exsolved γ–γ′ laths formed within the decomposed martensite laths.

Figure 9 shows a secondary electron image and Fig. 10b shows a fcc orientation map of a zoneless plessite particle, 60 μm × 35 μm, containing ~10 wt% Ni in the Kernouve H6 chondrite. As in the ataxites, the orientation of the fcc phase, which can be resolved with the EBSD technique, is essentially the same (considering the experimental accuracy of the EBSD technique of about ±1°) for most of the γ–γ′ phases along prior α_2 boundaries. Also apparent are a few other γ–γ′ regions that have a different orientation from the majority of the γ–γ′ and accounts for about 15% of the pixels indexed as fcc. All of the γ–γ′, including the misoriented γ–γ′, in the Kernouve metal particle has either the K-S or the N-W

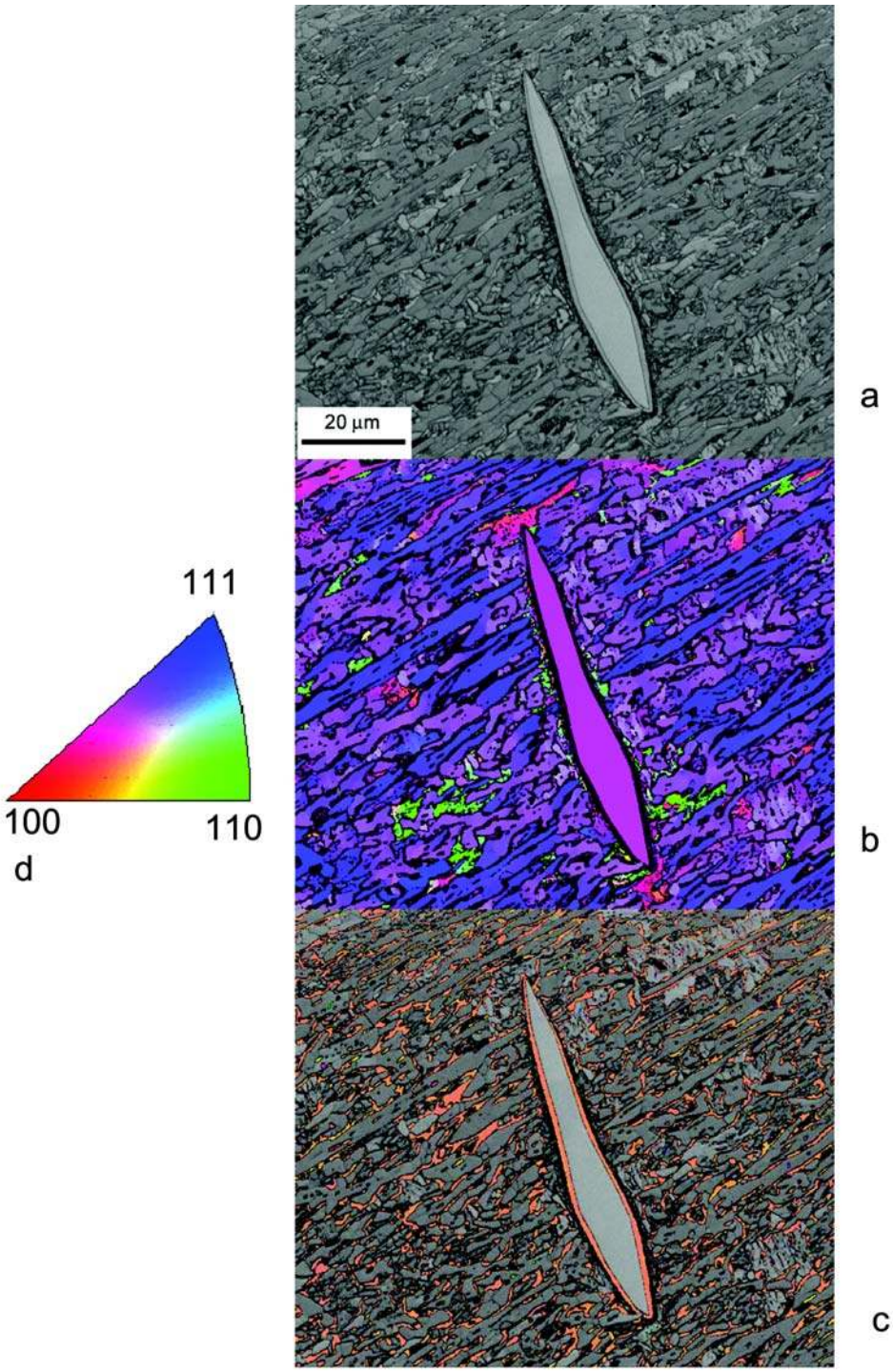

Fig. 4. EBSD orientation maps of five ataxites. a–c) Band contrast, kamacite (bcc) orientation, and taenite-tetrataenite (fcc) orientation maps of the Cape of Good Hope IVB ataxite. d) A typical color legend based on the stereographic triangle.

orientation relationship with the kamacite. This measurement suggests that the misoriented γ–γ′ is a result of exsolution from the super-saturated martensite. The bcc orientation maps show a number of different orientations for the kamacite reflecting the reaction path for the formation of the martensite (α_2) microstructure. Figure 12 shows the pole figures obtained from the orientation maps of Kernouve. Due to the small size of the metal particle, not all variants of the K-S, N-W, or G-T orientation relationships are present leading to a less well-defined pole figures as compared to Figs. 7 or 11. However, the pole figures are not substantially different than those shown for Cape of Good Hope or Carlton. These

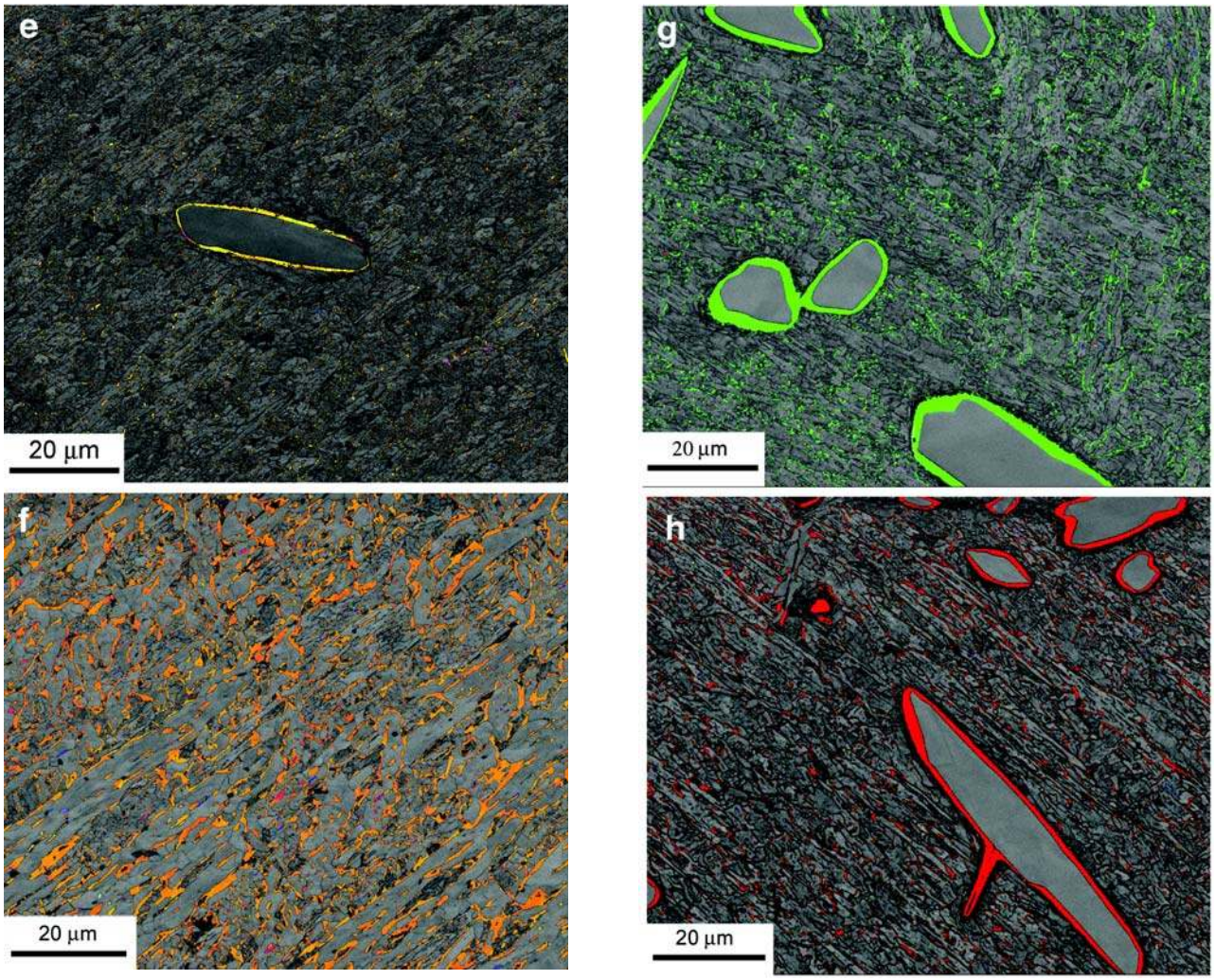

Fig. 4. *Continued.* e) Chinga. f) Hoba. g) Tawallah Valley and h) Weaver Mountains ataxites. The orientation of fcc taenite-tetrataenite in plessite and the high temperature single crystal fcc taenite are the same.

observations were reproduced after analysis of other zoneless plessite metal particles in Kernouve. The experimental pole figures shown in Fig. 11 for Carlton and Fig. 12 for Kernouve can be compared with the calculated pole figures shown in Fig. 8. The agreement between these figures shows that there is a strong orientation relation between the bcc and the fcc phases, and that these orientation relationships are consistent with the orientation relationships given in Table 2.

DISCUSSION

Orientation Relationships—Fcc Taenite

The results of this study using EBSD techniques show that the orientation of the taenite and/or tetrataenite (γ–γ') regions at the interfaces of prior α_2 laths is the same across the plessite structure and the same as the taenite single crystal of the meteorite. Therefore, the original taenite single crystal was retained at the interfaces of martensite laths during cooling after the formation of martensite, as described by Reaction 2. Nolze and Geist (2004), using EBSD, showed that for the meteorites Watson and Agpalilik, the fcc phase has the same orientation in plessite as in the fcc, which borders the kamacite of the Widmanstätten pattern. These results give further evidence of the formation of plessite by Reaction 2.

Nolze (2004) has shown quite convincingly that the orientations listed in Table 2 apply for either the exsolution of ferrite-kamacite from austenite-taenite or the exsolution of austenite-taenite from ferrite-kamacite. Thus, if the microstructure of the meteorite on cooling was fully martensite (α_2) any precipitation or exsolution of austenite-taenite from the supersaturated martensite (α_2) would result in austenite-taenite precipitates with all the required variants present. We cannot imagine how all the taenite would exsolve or precipitate from α_2 with the same orientation following a complete $\gamma \rightarrow \alpha_2$ transformation.

Therefore, the formation of plessite is inconsistent with Reaction 1, which is the classic mechanism proposed for type

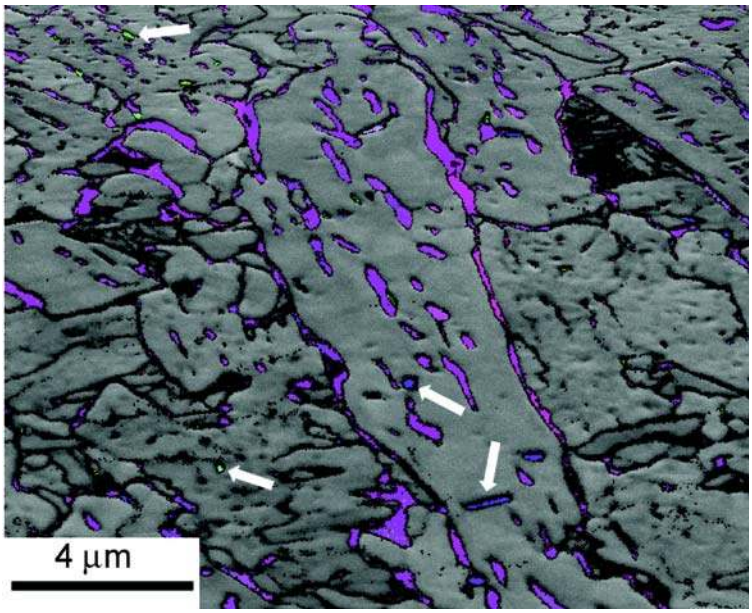

Fig. 5. A high-magnification taenite-tetrataenite (fcc) orientation map of Chinga. Taenite regions indicated by arrows have exsolved from martensite, α_2.

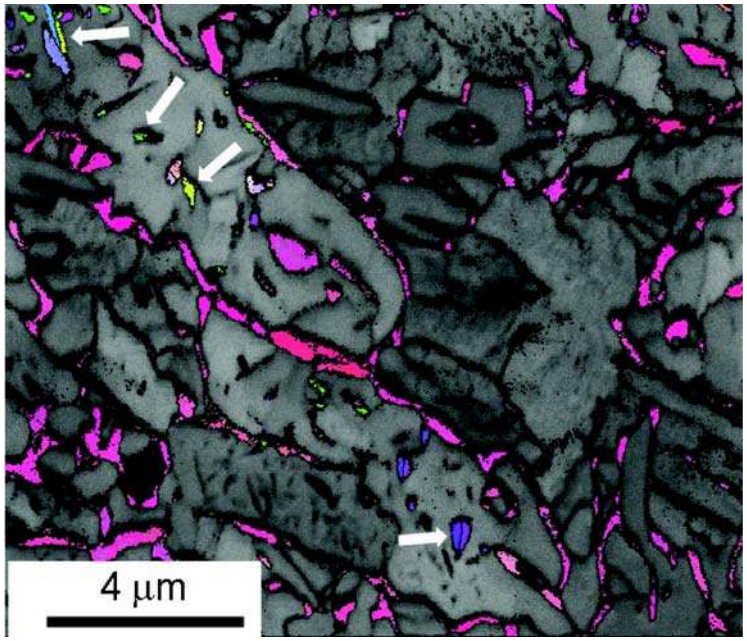

Fig. 6. A high-magnification taenite-tetrataenite (fcc) orientation map of Tawallah Valley. Taenite regions indicated by arrows have exsolved from martensite (α_2).

III plessite by Massalski et al. (1966), for plessite formation by Wood (1964), and for the continuum of plessite microstructures (duplex to black plessite) by Zhang et al. (1993). Yang and Goldstein (2005) proposed that Reaction 2 controls the formation of lower Ni plessite, such as duplex plessite. They argued that some of the parent taenite phase is retained to low cooling temperatures at the martensite lath boundaries. This transformation is consistent with the results of this study. However, Yang and Goldstein (2005) argued

Table 2. Kurdjumov-Sachs (K-S), Nishiyama-Wassermann (N-W), and Greninger-Troiano (G-T) orientation relationships between austenite and ferrite (taenite and kamacite).

Orientation	Plane	Direction
K-S	$\{111\}_\gamma \parallel \{110\}_\alpha$	$<1\text{–}10>_\gamma \parallel <1\text{–}11>_\alpha$
N-W	$\{111\}_\gamma \parallel \{110\}_\alpha$	$<0\text{–}11>_\gamma \parallel <001>_\alpha$
G-T	$\{111\}_\gamma$ ~1° to $\{110\}_\alpha$	$<\text{–}12\text{–}1>_\gamma$ ~2° $<1\text{–}10>_\alpha$

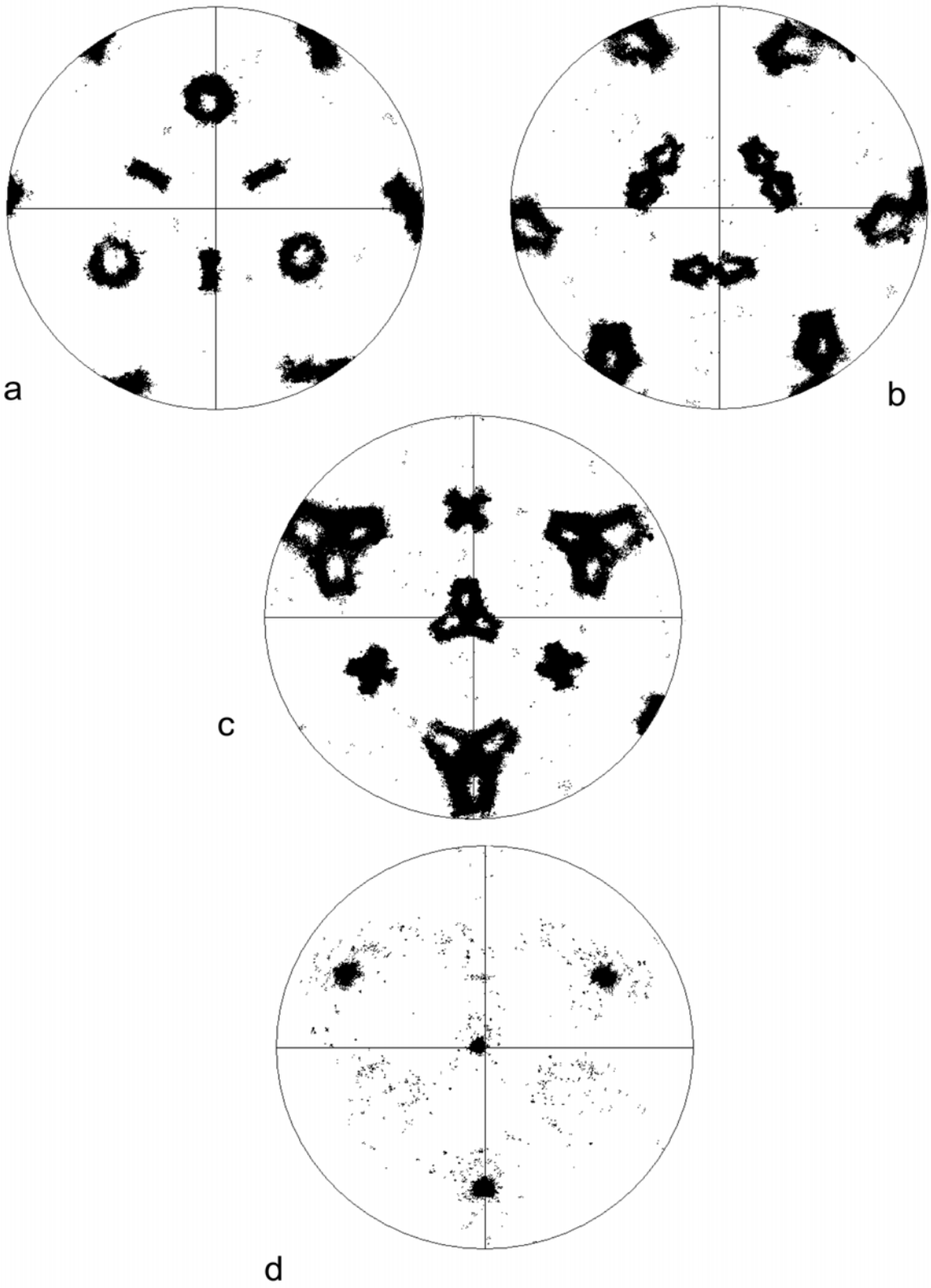

Fig. 7. Pole figures obtained from orientation maps of plessite in Tawallah Valley IVB. a) {100} pole figure for bcc; b) {111} pole figure for bcc; c) {110} pole figure for bcc; d) {111} pole figure for fcc.

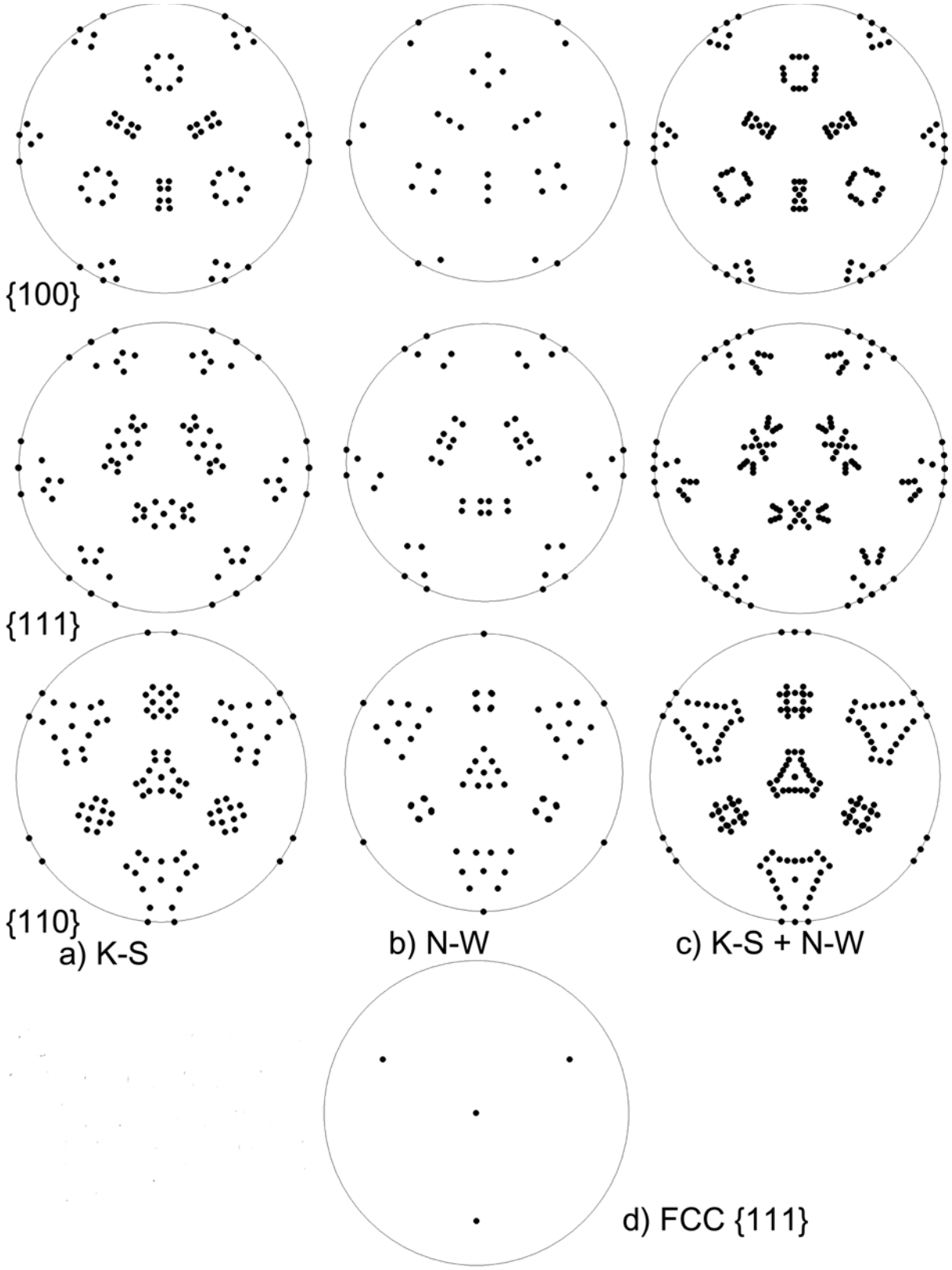

Fig. 8. Calculated {100}, {110}, and {111} pole figures of bcc kamacite for a single orientation of fcc taenite. a) Kurdjumov-Sachs (K-S) orientation; b) Nishiyama-Wassermann orientation (N-W); and c) combined K-S and N-W orientation.

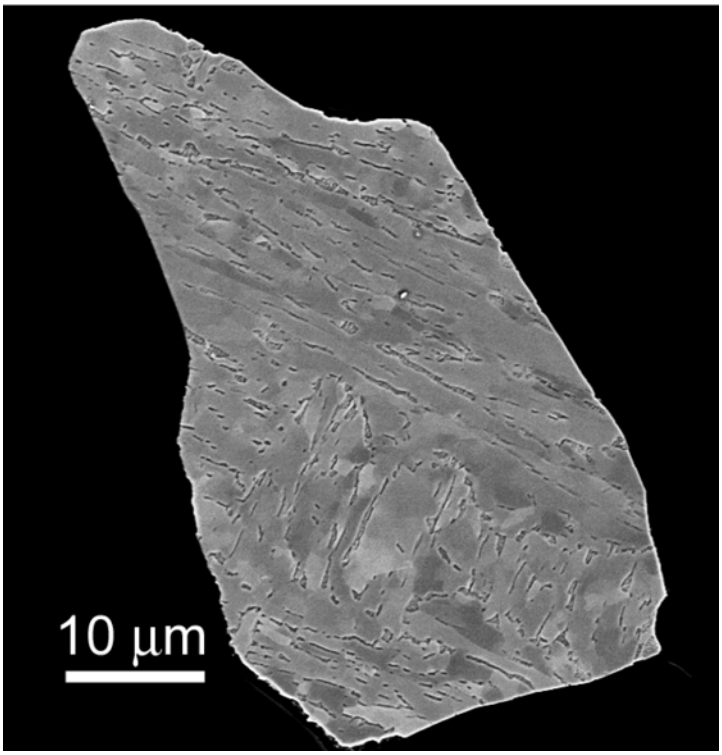

Fig. 9. A secondary electron image of a zoneless plessite particle in Kernouve, a H6 chondrite.

incorrectly that Reaction 1 controlled the formation of higher Ni plessite such as black plessite and that all the parent γ is converted to martensite (α_2) on cooling.

Some of the fine exsolved γ–γ′ within decomposed α_2 laths of plessite have different orientations (Figs. 5, 6, and 10a) than the original taenite single crystal of the meteorite. The varying orientations of the fine exsolved fcc within decomposed laths are a response to the decomposition of martensite α_2 laths at low temperature. In other words, the fine exsolved fcc within decomposed martensite laths formed by the reaction $\alpha_2 \rightarrow \alpha + \gamma$. Zhang et al. (1993) also proposed that exsolution lamellae of γ formed in prior martensite (α_2) laths and had a different orientation than that of the single crystal parent γ phase of the meteorite. A summary of the microstructural development of plessite as a function of original taenite Ni content and cooling history is given in a later section of the Discussion.

Orientation Relationships—Bcc Martensite—Kamacite

The bcc phase in each of the ataxites has a number of different orientations (e.g., Fig. 4b). The different orientations reflect the reaction path $\gamma \rightarrow \alpha_2\,(\text{bcc}) + \gamma$ in which the α_2 phase forms on the close-packed planes of the parent taenite. The experimental pole figures (Fig. 7) show reasonable agreement with the calculated pole figures of Fig. 8, demonstrating that the orientation relationship of the bcc and fcc phases can be described by some combination of N-W and K-S, as discussed by Nolze (2004). Nolze (2004) proposed that there is a spread in the orientation relationships that occur in the fcc/bcc system that extends from the K-S to the N-W orientation relationships and that the G-T orientation is intermediate between K-S and N-W. Unfortunately, K-S and G-T are not very far apart in angle (about 1° in axis and 2° in angle). As shown in Fig. 8, it is difficult to distinguish among K-S, N-W, or the G-T orientations. In summary, the bcc pole figures in Figs. 7 and 8 would only be expected when the bcc phase has transformed from a single orientation of the parent fcc phase. Similar results have been obtained by Stanford and Bate (2005) for transformations in α–β brass.

Plessite Formation in Meteorites

The EBSD measurements obtained from five ataxites, a IAB-IIICD iron, and a H6 chondrite, show that taenite and/or tetrataenite, at the interfaces of prior martensite laths ~10 to 18 wt% Ni, in plessite have the same orientation as the original high temperature taenite. These martensite laths form below the martensite start temperature, M_s, as the meteorite cools in its parent body. Reaction 2, as postulated by Yang and Goldstein (2005) for the formation of the Widmanstätten pattern in low P iron meteorites, also controls the formation of plessite.

During cooling, a specific meteorite metal particle, for

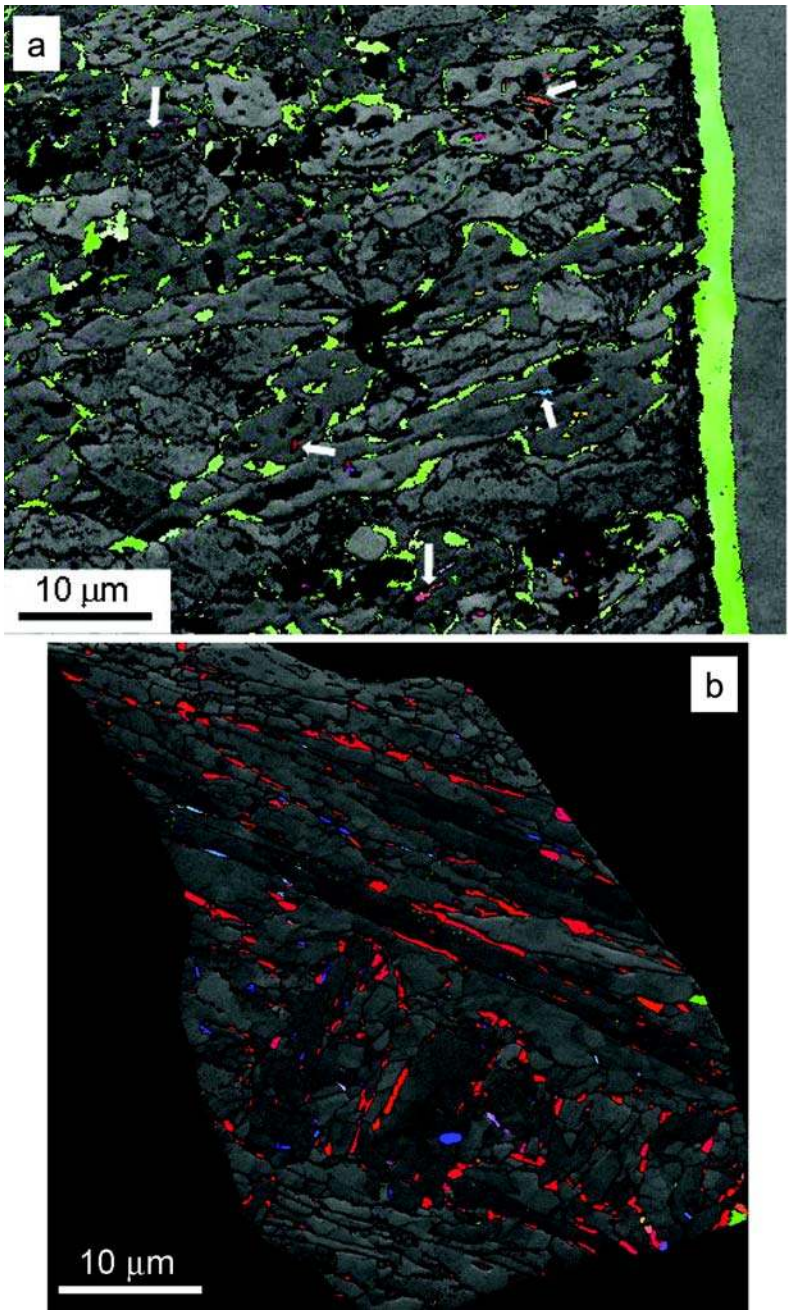

Fig. 10. Fcc orientation maps of a) Carlton IAB-IIICD and b) zoneless plessite particle in Kernouve, a H6 chondrite. A Widmanstätten kamacite/taenite boundary in Carlton is shown in (a). The gray, featureless phase on the right hand side of (a) is Widmanstätten kamacite.

example, ~9 wt% Ni (Fig. 2), the Ni content of the taenite that surrounds the growing kamacite phase will have an Ni gradient from approximately 50 wt% at the kamacite/taenite border to a Ni content as low as the bulk Ni content of the metal particle. During cooling to lower temperatures, the various local Ni content regions of the taenite pass through the martensite start, M_s, at different temperatures, decreasing with increasing Ni content. Therefore, the plessite microstructure is controlled by the Ni content. Plessite forms according to the general scheme given in the next paragraph.

Taenite cools from high temperature through the M_s temperature (see Fig. 2). Taenite starts to transform to martensite (α_2) which has the same Ni content. The α_2 forms on the close-packed planes of fcc as given by the K-S or N-W relations. Untransformed fcc γ phase borders the martensite (α_2) and retains the original orientation of the parent taenite.

The Ni content of the γ phase at the martensite boundary will increase with decreasing temperature in order to maintain equilibrium with bcc α phase which transformed from the martensite (α_2) at the γ/α_2 boundary (see Fig 2). The

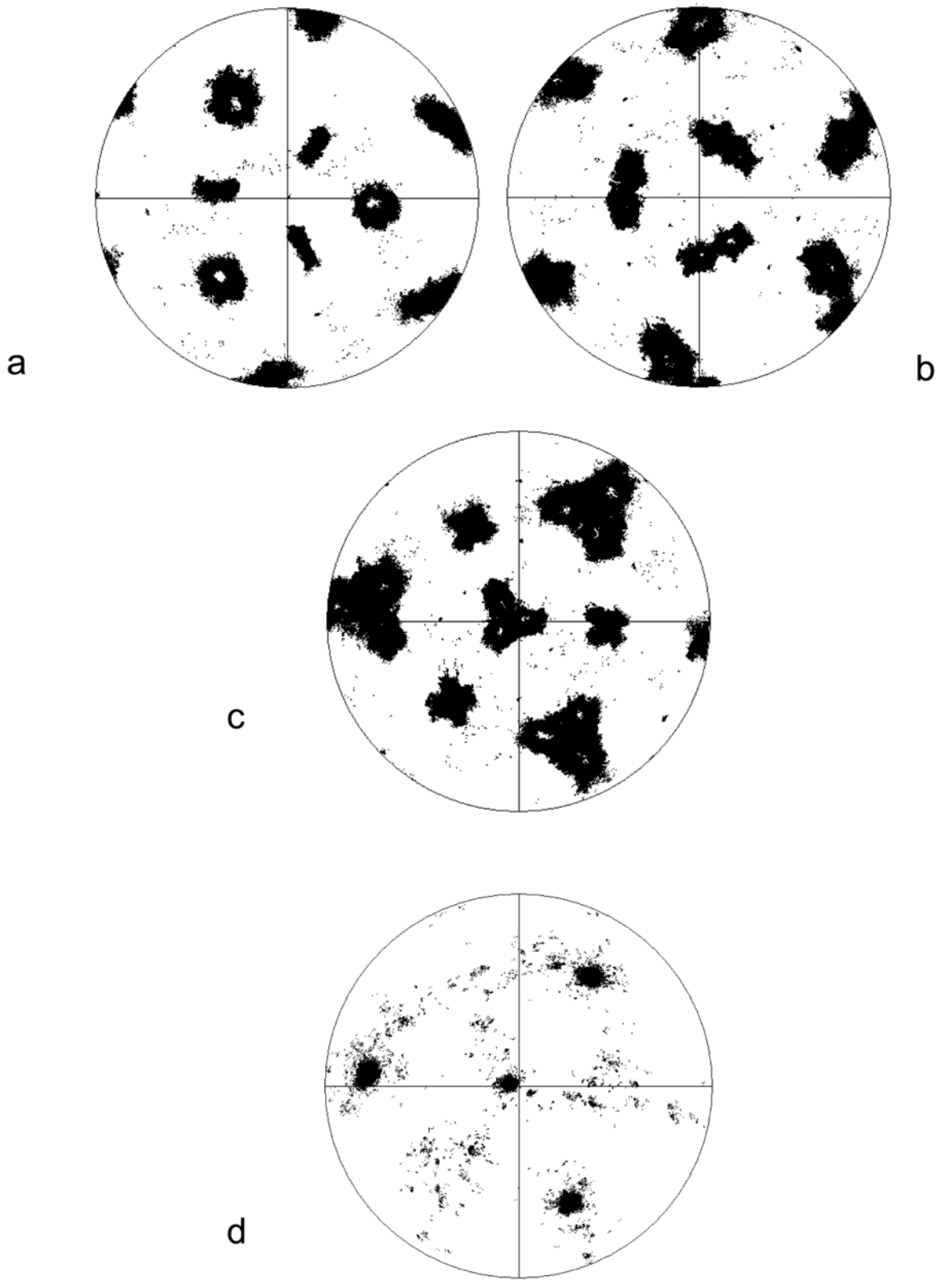

Fig. 11. Poles obtained from orientation maps of plessite in Carlton IAB-IIICD. a) {100} pole figure for bcc; b) {111} pole figure for bcc; c) {110} pole figure for bcc; d) {111} pole figure for fcc.

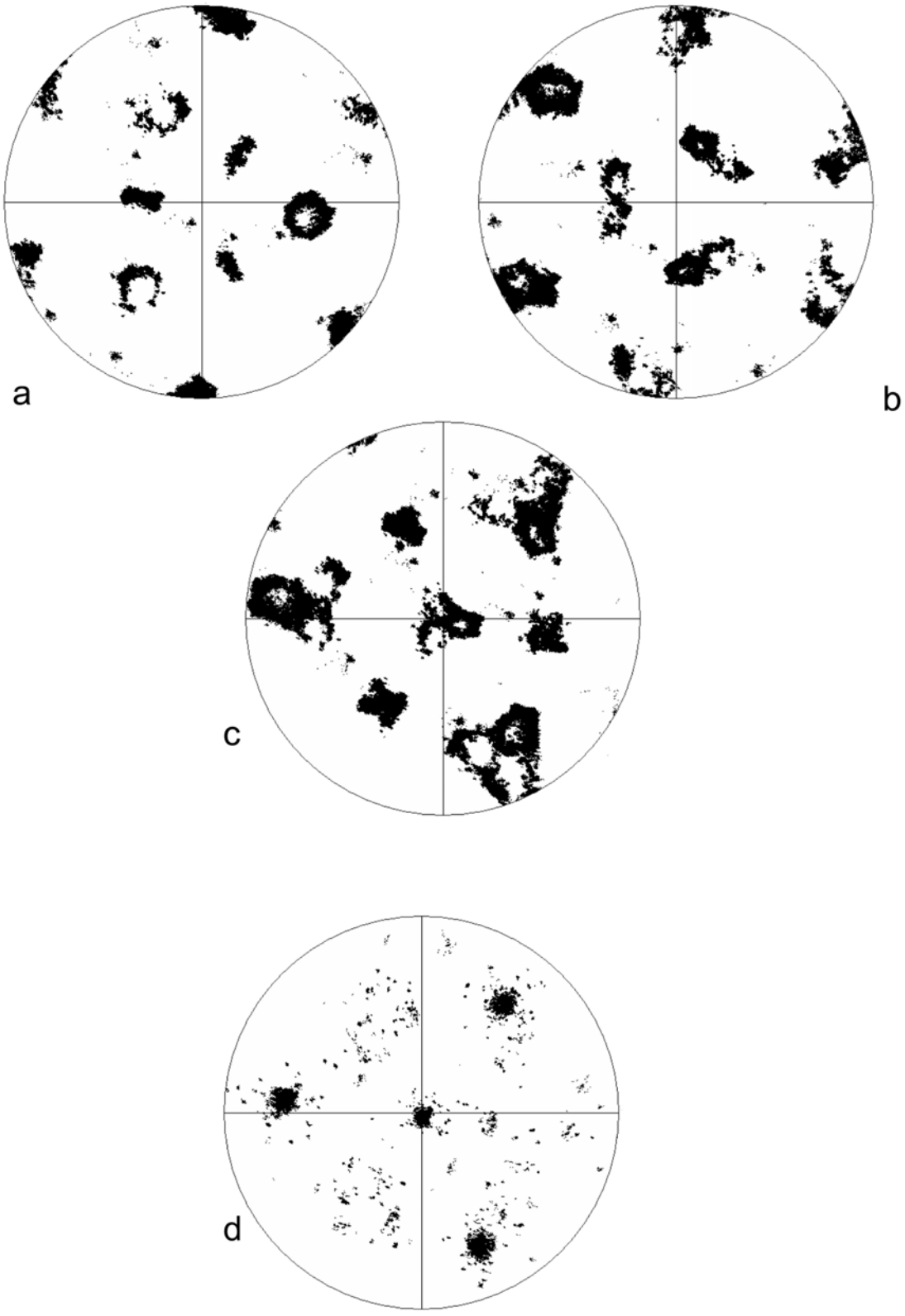

Fig. 12. Pole figures obtained from orientation maps of a zoneless plessite particle in Kernouve, a H6 chondrite. a) {100} pole figure for bcc; b) {111} pole figure for bcc; c) {110} pole figure for bcc; d) {111} pole figure for fcc.

increased Ni in the taenite at the martensite boundary is supplied by diffusion through the α_2 (martensite). At lower temperatures, more of the martensite (α_2) is converted to bcc α (kamacite) phase. The α phase which forms has the same specific orientation relationships, (K-S and/or N-W) as the martensite had with the parent taenite. With further cooling more bcc α phase forms as martensite, α_2, decomposes. This process continues until the final cooling temperature. At low temperatures, diffusion of Ni through the α_2, martensite, may decrease to such an extent that the martensite is supersaturated with Ni with respect to the equilibrium Ni content of α, kamacite. If supersaturation occurs, γ may exsolve in the martensite by the reaction $\alpha_2 \rightarrow \alpha + \gamma$, as observed for the ataxites and the Carlton meteorite (Figs. 5, 6, and 10a). At the final cooling temperature, <200 °C, the taenite and/or tetrataenite at the martensite borders will have the same crystallographic orientation as the parent taenite and a composition given by the $\gamma/(\alpha + \gamma)$ phase boundary of the Fe-Ni phase diagram (Fig. 2). The kamacite of the plessite microstructure has a crystallographic relationships to the high temperature taenite phase as given by the K-S or N-W relations and the exsolved taenite in the prior martensite has a direct crystallographic orientation to the martensite parent phase. The following paragraphs describe the formation of the plessite microstructure at Ni contents of ~10–13, 13–18, and >20 wt%. These Ni contents cover various types of plessite, duplex, and black plessite (type III plessite) and martensitic plessite (type II plessite).

For metal of approximately 10 wt% Ni, similar to that of the zoneless plessite particle in Kernouve and in the composition range of duplex plessite (<13–14 wt% Ni), the M_s temperature is above 400 °C and the martensite forms as laths in the taenite matrix. The Ni content of the fcc taenite at the α_2 boundary follows the $\gamma/(\alpha + \gamma)$ boundary of the Fe-Ni Phase diagram (Fig. 2). The Ni content of the α_2 phase will follow the $\alpha/(\alpha + \gamma)$ boundary and Ni will diffuse from the α_2 phase to the surrounding γ phase. Below 400 °C, the Ni content of the fcc taenite at the α_2 boundary approaches FeNi, as γ_2, and orders to γ'' below 320 °C. Temperatures are high enough that diffusion of Ni through α_2 is complete and little or no γ exsolves in the α_2 phase. The reaction path for duplex plessite is given by Reaction 2.

For metal of >13–14 wt% Ni to ~18 wt% Ni, in the composition range of black plessite, and overlapping the Ni content of the IVB irons (15.6–18 wt% Ni), the M_s temperature is below 400 °C and is as low as 300 °C (Fig. 2). The martensite forms as laths in the taenite matrix. In this low temperature range, the Ni content of the taenite at the α_2 boundary follows the γ_2 phase boundary and will order to γ'' below 320 °C. The Ni content of the α_2 phase will follow the $\alpha/(\alpha + \gamma)$ boundary and Ni will decrease by diffusing from the α_2 phase to the surrounding γ phase. However, as the Ni content of the metal, from which black plessite forms, increases, the M_s decreases. The diffusion of Ni to the surrounding γ phase will also decrease due to the low temperature. In order for the Ni content of the α_2 phase to decrease according to the $\alpha/(\alpha + \gamma)$ boundary of the Fe-Ni phase diagram, γ phase precipitates in the matrix of the α_2 as tetrataenite, ordered FeNi, γ'', below the ordering temperature of 320 °C. The reaction path for black plessite is also given by Reaction 2 where ordered tetrataenite (γ'') forms at both the martensite (α_2) boundary and in the matrix of the martensite. As discussed previously, the diffraction pattern from γ'' is indistinguishable from that of γ taenite.

In summary, plessite of Ni contents from ~10 to 18 wt% forms by Reaction 2, where γ can also be ordered γ'', in iron, stony-iron, and chondritic metal. The γ and/or tetrataenite γ'' phase observed between martensite laths has the same orientation as the original single crystal taenite of the meteorite.

For metal of ~20 to ~28 Ni (Fig. 1d), as discussed by Zhang et al. (1993), only a thin region of γ phase is observed at the interface between martensite plates in plessite regions with Ni contents of ~20 wt% or higher. Martensite forms below ~250 °C in a plate shape in the taenite matrix. At this low temperature, little Ni diffusion can occur in the α_2 martensite that forms. Therefore, as shown by Zhang et al. (1993), 10–100 nm γ exsolution plates form in α_2 martensite at low temperatures, <~300 °C by the reaction $\alpha_2 \rightarrow \alpha + \gamma''$. The γ plates have N-W, K-S, or G-T orientations with respect to the α_2 martensite. For type II plessite, the reaction path is also given by reaction 2) $\gamma \rightarrow \alpha_2 + \gamma \rightarrow \alpha + \gamma$ where ordered tetrataenite, γ'', forms at both the martensite, α_2, boundary and in the matrix of the martensite, α_2. In this type of plessite, more of the γ'' phase formed within the martensite than remains at the boundary of the martensite plates.

The zoneless plessite metal particles in Kernouve are of particular interest. Reisener and Goldstein (2003) postulate that zoneless plessite forms by Reaction 1 in which monocrystalline parent taenite particles are slowly cooled. If this reaction controlled the process, the γ–γ'' would have a number of different orientations (K-S or N-W) with respect to the bcc prior martensite. However, the EBSD orientation maps (Fig. 10b) show that almost all the γ–γ'' regions have the same orientation throughout the microstructure. Such a result can only be explained by the presence of retained taenite from the monocrystalline parent taenite phase during the formation of plessite below the martensite start temperature. Reaction 2 controls plessite formation in zoneless plessite of ~10 wt% Ni (Fig. 7b).

CONCLUSIONS

The orientation of the fcc taenite and/or tetrataenite regions at the interfaces of prior α_2 laths in the plessite microstructure, as observed by electron backscatter diffraction (EBSD) techniques for five ataxites, the Carlton IAB-IIICD iron, and zoneless plessite in the Kernouve H6

chondrite, is 1) the same all across the plessite structure, and 2) the same as the original taenite single crystal metal within the meteorite. The γ–γ' phase at the interfaces of martensite laths in the plessite microstructure was retained during cooling after formation of martensite according the reaction $\gamma \rightarrow \alpha_2 + \gamma \rightarrow \alpha + \gamma$. This reaction is applicable for duplex and black plessite in iron, stony-iron, and chondritic metal. The EBSD orientation data are inconsistent with the reaction, $\gamma \rightarrow \alpha_2 \rightarrow \alpha + \gamma$, the classical reaction proposed by previous investigators. Some of the fine exsolved γ–γ' precipitates within the α_2 martensite have varying orientations with respect to the original taenite of the metal. These precipitates probably formed by the reaction $\alpha_2 \rightarrow \alpha + \gamma$.

The bcc phase in plessite has a number of different orientations. These orientations reflect the reaction path γ (fcc) $\rightarrow \alpha_2$ (bcc) in which the α_2 phase forms on the close-packed planes of the parent taenite phase according to any one of the established orientation relationships (K-S, N-W, or G-T) for the fcc to bcc transformation.

Acknowledgments–The authors acknowledge the financial support from NASA through grant NAG5-11778. Sandia is a multiprogram laboratory operated by Sandia Corporation, a Lockheed Martin Company, for the United States Department of Energy (DOE) under contract DE-AC0494AL85000.

Editorial Handling—Dr. Edward Scott

REFERENCES

Albertsen J. G. 1981. Tetragonal lattice of tetrataenite (ordered Fe-Ni, 50-50) from four meteorites. *Physica Scripta* 23:301–306.

Buchwald V. F. 1975. *Handbook of iron meteorites: Their history, distribution, composition and structure,* vol. 1. Berkeley: University of California Press. 262 p.

Campbell A. J. and Humayun M. 2005. Compositions of group IVB iron meteorites and their parent melt. *Geochimica et Cosmochimica Acta* 69:4733–4744.

Guo Z., Lee C. S., and Morris J. W. 2004. On coherent transformations in steel. *Acta Materialia* 52:5511–5518.

He Y. L., Godet S., and Jonas J. J. 2005. Representation of misorientations in Rodrigues-Frank space: Application to the Bain, Kurdjumov-Sachs, Nishiyama-Wassermann, and Pitsch orientation relationships in the Gibeon meteorite. *Acta Materialia* 53:1179–1190.

Humphreys F. J., Huang Y., Brough I., and Harris C. 1999. Electron backscatter diffraction of grain and subgrain structures-resolution concerns. *Journal of Microscopy* 195:212–216.

Humphreys F. J. 2001. Grain and subgrain characterization by electron backscatter diffraction. *Journal of Materials Science* 36: 3833–3854.

Hutchinson B. and Hagström J. Forthcoming. Austentite decomposition structures in the Gibeon meteorite. *Metallurgical and Materials Transactions A*.

Jago R. A. 1981. Plessite formation and morphology in ataxites and plessitic octahedrites. *Geochimica et Cosmochimica Acta* 45: 1835–1853.

Massalski T. B., Park F. R., and Vassamillet L. F. 1966. Speculations about plessite. *Geochimica et Cosmochimica Acta* 30:649–662.

Nolze G. and Geist V. 2004. A new method for the investigation of orientation relationships in meteoritic plessite. *Crystallographic Research and Technology* 39:343–352.

Nolze G. 2004. Characterization of the fcc/bcc oreintation relationship by EBSD using pole figures and variants. *Zeitschrift für Metallkunde* 95:744–755.

Novotny P. M., Goldstein J. I., and Williams D. B. 1982. Analytical electron microscope study of eight ataxites. *Geochimica et Cosmochimica Acta* 46:2461–2469.

Reisener R. J. and Goldstein J. I. 2003. Ordinary chondrite metallography: Part 2. Formation of zoned and unzoned metal particles in relatively unshocked H, L, and LL chondrites. *Meteoritics & Planetary Science* 38:1679–96.

Schwartz A. J., Kumar M., and Adams B. L. 2000. *Electron backscatter diffraction in materials science.* New York: Kluwer-Academic/Plenum Publishers. 350 p.

Sivel V. G. M., Tichelaar F. D., Mohadi H., Alkemade P. F. A., and Zanderbergen H. W. 2005. Crystallographic analysis of thin specimens. *Journal of Microscopy* 218:113–124.

Stanford N. and Bate P. S. 2005. Crystallographic variant selection in alpha-gamma brass. *Acta Materialia* 53:859–867.

Yang J. and Goldstein J. I. 2005. The formation of the Widmanstätten structure in meteorites. *Meteoritics & Planetary Science* 40:239–253.

Zhang J., Williams D. B., and Goldstein J. I. 1993. The microstructure and formation of duplex and black plessite in iron meteorites. *Geochimica et Cosmochimica Acta* 57:3725–3735.